
CONDITIONING GENERATIVE LATENT OPTIMIZATION FOR SPARSE-VIEW CT IMAGE RECONSTRUCTION

Thomas Braure¹, Delphine Lazaro², David Hateau¹, Vincent Brandon¹, and Kévin Ginsburger¹

¹CEA DIF, 91297 Arpajon Cedex, France

²CEA LIST, 91191 Gif-sur-Yvette Cedex, France

May 1, 2024

ABSTRACT

Computed Tomography (CT) is a prominent example of Imaging Inverse Problem (IIP), highlighting the unrivaled performances of data-driven methods in degraded measurements setups like sparse X-ray projections. Although a significant proportion of deep learning approaches benefit from large supervised datasets to directly map experimental measurements to medical scans, they cannot generalize to new experimental setups, e.g. changes concerning source/detector specifications and/or the acquisition geometry. In contrast, fully unsupervised techniques, most notably using conditioned Score-based Generative Models (cSGM) with Manifold Constrained Gradients (MCG), have recently demonstrated similar or better performances compared to supervised approaches to solve IIPs while being flexible at test time regarding the experimental setup. However, their use cases are limited as they need considerable amounts of training data to have good generalization properties. Another unsupervised approach taking advantage of the implicit natural bias of deep convolutional networks, Deep Image Prior (DIP), has recently been adapted to solve low-dose and sparse CT by reparameterizing the reconstruction optimization problem. Although this methodology does not require any training dataset, it enforces a weaker prior on the reconstructions when compared to data-driven methods. To fill the gap between these two strategies, we propose an unsupervised conditional approach to the Generative Latent Optimization framework (cGLO), in which a decoder is used for reconstruction purposes, by performing Generative Latent Optimization with a loss function directly comparing simulated measurements from proposed reconstructions to experimental measurements. Similarly to DIP, without any training dataset, cGLO benefits from the structural bias of a decoder network. However, the prior is further reinforced as the effect of a likelihood objective shared between multiple slices being reconstructed simultaneously through the same decoder network. In addition, the parameters of the decoder may be initialized on an unsupervised, and eventually very small, training dataset to enhance the reconstruction. The resulting approach is tested on full-dose sparse-view CT using multiple training dataset sizes and varying numbers of viewing angles. Our method demonstrates better reconstruction Structural SIMilarity (SSIM) compared to the state-of-the-art MCG strategy, between +0.041 and +0.134. cGLO also shows an increasing performance advantage over MCG for smaller training datasets, reaching a +2.58 dB Peak Signal to Noise Ratio (PSNR) gain. When no training dataset is available, our method also outperforms the DIP approach with at least +1.52 dB PSNR advantage, and especially with fewer viewing angles reaching +3.15 dB. Furthermore, cGLO does not require any backward operator and could expand use cases, like recent developments of score-based models, to non-linear IIPs.

1 Introduction

Imaging Inverse Problems (IIPs) are a large and swiftly growing area of research. IIPs cover a large variety of applications, ranging from generic image processing topics such as denoising, super-resolution and deconvolution to more specific domains usually involving the characterization of a system of interest from indirect observations. In

this latter case, the problem of reconstructing scans from medical imaging devices such as Computed Tomography (CT), Magnetic Resonance Imaging (MRI) and Positron Emission Tomography (PET) offers major challenges yet to be solved. Among those, CT reconstruction is a prime example of medical IIPs. The issue of delivered doses to patients has led to sparser sets of X-ray projection angles and/or a decrease in X-ray intensities resulting in noisier, less contrasted and detailed projection images. When using such degraded measurement setups, reconstructions obtained by conventional numerical methods, e.g. Filtered Back-Projection (FBP) [1], are severely worsened.

Recent progress have been made using deep learning approaches for CT reconstruction. However, a large part of these novel data-driven methods employ a supervised training setup [2, 3, 4, 5, 6, 7, 8]. In supervised training pairs, ground truths consist of 3D volumetric scans reconstructed from conventional techniques such as the well-known FBP algorithm, using high-dose and densely sampled X-ray measurements. A degraded set of measurements is associated to each ground truth. These are usually obtained by taking a subset of the original X-ray projections (full-dose sparse view CT or sparse CT) and/or by adding noise to simulate dose reduction (low-dose CT). Building such supervised datasets thus implies that a fixed physical model has been employed for all training pairs, which must be identical to the one used for inference. In other words, supervised reconstruction strategies need new training whenever the acquisition process changes. This can be problematic when the viewing angles, X-ray spectrum or beam geometry vary. To circumvent this drawback, several unsupervised strategies have recently been introduced.

Current approaches dealing with ill-posed IIPs in an unsupervised way are mostly based on the use of generative models. As such, the Generative Adversarial Networks (GANs) [9] are largely employed for unsupervised reconstruction tasks [10]. As serious contenders to GANs, Diffusion Models (DMs) [11, 12] have gained a lot of attention in the past few years, as recent improvements have led to the generation of high-quality image samples without requiring a complex adversarial optimization [13, 14, 15, 16]. The basic principle of DMs is to add noise of increasing intensity to data during the training process and learn to reverse this process, i.e. starting from random noise and producing a sample from the data distribution through successive denoisings. In the continuous approach [17], the discrete sequence of noise levels is replaced by a continuum of distributions progressively diffusing data points into random noise following a Stochastic Differential Equation (SDE) describing a markovian diffusion process. The reverse-time SDE is approximated with a time-dependent neural network estimating the gradient of the prior likelihood, also called the score function. Using standard iterative sampling techniques then leads to generative capability. Following this general strategy, two types of SDE formulations can be distinguished: the variance preserving Denoising Diffusion Probabilistic Models (DDPMs) [12, 18] and the variance exploding Score-matching Generative Models (SGMs) [11, 17, 19]. In particular, recent works involving DMs have proven strong performances in solving IIPs [20, 21, 22, 23, 24] and more specifically, sparse CT reconstruction [23, 25, 26]. Both GANs and DMs are very efficient to learn unconditional prior distributions on slices of 3D reconstructed volumes. However, difficulties arise when a conditional sampling is needed to reconstruct slices from experimental X-ray projections. Various strategies have been proposed to deal with this conditional sampling issue.

GAN inversion approaches [10] start from a *trained and fixed* decoder, and aim at estimating the latent code corresponding to a given observation. The inversion process can either be learning-based [27, 28], e.g. learning an encoder to inverse the decoder, or optimization-based where the optimization problem is solved by finding the latent code minimizing the given objective function [29, 30], or both [31, 32, 33]. Other approaches using a parameterization of the latent space have been proposed, where the decoder and the encoder are jointly learned using an adversarial process [34, 35, 36, 37, 38, 39, 40]. Similarly to GANs, conditional inference using DMs is an open field of research. It is generally performed using a biased sampling of the posterior distribution to generate approximate samples from a stochastic process conditioned to experimental measurements. For instance, in the context of sparse CT reconstruction, conditioning an SGM (cSGM) to X-ray projections, as in [25], involves computing the FBP on experimental measurements completed with simulated measurements from the candidate reconstruction, i.e. a proximal projection step throwing the sample path off the data manifold according to [26]. In the latter, a Manifold Constraint on the Gradient (MCG) is enforced during the sampling process as an additional correction term resulting in more robust reconstructions. While both these methods are restricted to linear IIPs, a recent work from Chung et al. [23], known as Deep Posterior Sampling (DPS), has extended the use cases of DMs to noisy non-linear problems. As interestingly noted in [23], DPS is equivalent to MCG in *noiseless* configurations, e.g. full-dose sparse view CT which is the application of interest in this paper.

Unsupervised generative models require large amounts of training data, which can be difficult to collect. Furthermore, while these approaches have good generalization given sufficient training data, in practice it is not clear how much is necessary. To address this issue, Ulyanov et al. proposed a method specific to IIP solving, Deep Image Prior (DIP) [41]. They showed that the structure of a deep convolutional network inherently captures a significant amount of low-level image statistics without any learning. That is to say, it induces an implicit structural bias, i.e. a prior. DIP uses a randomly initialized U-Net architecture [42], and a fixed input noise. The network weights can then be optimized to solve any ill-posed IIP with known forward model, such as inpainting or super-resolution. It has been shown that this

IIP reparameterization, when optimized with gradient descent, hierarchically reconstructs from low to high frequencies, i.e. converging faster towards "natural images" than noise [43, 44]. The method has recently been adapted in [45] to solve low-dose and sparse CT reconstruction. While this strategy showed good results on use cases with missing or small datasets, it imposes a quite rough prior which cannot compete with the reconstruction performances of its data-driven counterparts in degraded measurement setups.

This paper bridges the gap between, on one side, data-hungry generative models offering strong priors, and data-free methods providing weak priors on the other side, by proposing a reconstruction method readily usable *with* or *without* training data. Our method is a conditional version of the Generative Latent Optimization (GLO) [46] framework. GLO was designed as a generative model attempting to produce competitive results when compared to GANs without using an adversarial training protocol. Models building on GLO are focused on improving its generative characteristics [47, 48, 49], and to the best of our knowledge, it has never been conditioned to solve IIPs. Indeed, exploring or sampling the latent space of GLO is not trivial [48, 49], thus making it difficult to apply standard GAN inversion technique to directly solve IIPs. Instead, in this work, GLO is used to reparameterize the IIP. Similarly to DIP, our conditioned version of GLO (cGLO) exploits the inherent structural prior induced by a convolutional decoder, allowing reconstructions without any training dataset. However, contrary to DIP, cGLO can benefit from a shared objective by reconstructing multiple slices at the same time and an unsupervised training dataset of any size to initialize its decoder weights, resulting in greatly improved reconstruction results. The higher the quantity of training data is used for initialization, the stronger the induced prior is.

The paper is organized as follows. Section 2 details our cGLO method, built upon the reparameterization strategy of DIP and the framework of GLO. Consequently, both DIP and GLO are introduced beforehand. Section 3 describes the experimental setups used to benchmark our method on the full-dose sparse view CT reconstruction task. These setups correspond to situations with sparse or abundant training data. The section ends with implementation details regarding network architecture and hyperparameter values. Our method cGLO is then compared, in Section 4, through quantitative and qualitative results for two distinct scenarios. It is first compared to DIP and FBP *without* any training data available. Then it is compared to cSGM and MCG *with* prior unsupervised training on datasets of varying sizes. The paper concludes with a summary and suggestions for future works in Section 5.

2 Method

The method we propose here builds on the framework described by GLO and on the DIP approach which is a method dedicated to solve IIPs through reparameterization of the objective. This reformulation of DIP is detailed for a denoising task and for its adaptation to sparse CT reconstruction. Then, GLO and the concept of latent optimization are presented in the context of *unconditioned* generation, i.e. not directly applicable to IIP solving. Finally, our method cGLO is described with an objective function corresponding to the experiments conducted in this paper, i.e. full-dose sparse CT. In addition, a formalism for the Radon transform/CT and for score-based methods (SGM, cSGM and MCG) is given in Appendix A and B.

2.1 Deep Image Prior (DIP)

Ulyanov et al. [41] introduced DIP to solve classic IIPs such as denoising and super-resolution. The core idea of DIP is to regularize IIPs by taking advantage of the structural bias of a U-Net [42] f_θ parameterized with a set of weights θ . It operates through two mechanisms: reparameterization and early stopping (*ES*). For instance, in the case of denoising, the optimization problem is reparameterized as:

$$x^* = \{f_{\theta^*}(z) \mid \theta^* = \arg \min_{\theta} \|f_\theta(z) - (x_0 + \eta)\|_2^2\} \quad (1)$$

where x_0 is the initial image perturbed with unknown white noise η and z is a fixed white noise with the same dimensions as x_0 . Experiments in [41] showed that given sufficient capacity and time/iterations, via gradient descent, the randomly initialized and over-parameterized U-Net can fit the output signal almost perfectly, including the noise η . However, Ulyanov et al. [41] showed that the weights descent sequence $\theta_1, \dots, \theta_N$, with $f_{\theta_N} \approx x_0 + \eta$, contains an early stopping point θ_{ES} , such that $f_{\theta_{ES}} \approx x_0$. This phenomenon has been proven to be a consequence of the structure of the generative network, more specifically the convolutional and upsampling layers [43, 44]. They induce a spectral bias in which the decoder learns to construct the image from low to high frequencies, meaning that with an appropriate choice of *ES*, one can prevent the decoder from fitting the high frequency perturbations.

This methodology has recently been tailored to reconstruct 3D CT volumes by Baguer et al. [45], using an adaptation of Eq. (1) further regularized with Total Variation (TV):

$$x^* = \{f_{\theta^*}(z) \mid \theta^* = \arg \min_{\theta} \|\mathcal{T}_{\phi_e} \circ f_{\theta}(z) - y_{\phi_e}\|_2^2 + \alpha \text{TV} \circ f_{\theta}(z)\} \quad (2)$$

where \mathcal{T}_{ϕ_e} is the Radon transform sampled on experimental viewing angles ϕ_e , y_{ϕ_e} are the experimental measurements and α is a hyper-parameter balancing the regularization. In this formulation, the issue of finding an appropriate early stopping for denoising is replaced with the necessity to find an optimal value for α , depending on the ill-posedness of the IIP at hand.

Further experiments in [45] showed improvements by initializing the decoder weights using the result x_s of a supervised method, e.g. Learned Primal-Dual reconstruction [4]:

$$\theta_0 = \arg \min_{\theta} \|f_{\theta}(z) - x_s\|_2^2 \quad (3)$$

However, replacing random weights of the decoder with such a supervised initialization restricts the applicability of the approach to the supervised use case, i.e. fixed acquisition parameters. To avoid this, Baguer et al. use for this initialization a reconstruction computed with standard data-free techniques instead, e.g. FBP.

2.2 Generative Latent Optimization (GLO)

The GLO technique uses a decoder network and a set of *learnable* unit noise vectors, i.e. latent codes, where each code is associated to a single individual of the unsupervised training dataset. During training, the gradient is back-propagated both on the weights of the decoder and on the latent codes.

Formally it consists in mapping one freely *learned* unit latent vector z_i to each image x_i of a given dataset $X = \{x_1, \dots, x_N\}$, through a decoder network f_{θ} with parameters θ , e.g. a DCGAN [50]. With gradient descent, it comes to jointly learn decoder network parameters and latent codes $Z = \{z_1, \dots, z_N\}$, both randomly initialized, with the objective function:

$$Z^*, \theta^* = \arg \min_{Z, \theta} \frac{1}{N} \sum_{i=1}^N \|f_{\theta}(z_i) - x_i\|_2^2 \quad s.t. \quad \|z_i\|_2 = 1 \quad (4)$$

It is mentioned in [46] that, as is conventionally done for training GANs, vectors sampled from an n-dimensional normal distribution are close to the surface of an n-sphere with radius \sqrt{n} . Following this idea, Bojanowski et al. propose to constrain the latent vectors to the unit n-sphere. It facilitates the exploration of the latent space and allows data transformation via geodesic interpolation. This constraint does not deteriorates the optimization and is numerically simple as it consists in projecting the latent vectors onto the unit n-sphere, i.e. normalizing, after each back-propagation.

Experiments in [46] and [47] have shown that the GLO approach does not suffer from mode collapse and significantly outperform GANs when trained on small datasets. However, like Variational Auto-Encoders (VAE) [51], the quality of generated samples deteriorates when the data variability overcomes the network capacity [52].

2.3 Conditioning GLO (cGLO)

Following GAN inversion literature [10], one could try to search the latent space to find the best candidate latent vector so that the output of the decoder is close to experimental observations. However, attempting to invert GLO, i.e. sampling or exploring the manifold entailed by latent vectors learned through Eq. (4), is not straightforward [48, 49]. The latent vectors are not uniformly distributed on the surface of the n-sphere. Furthermore, the decoder generation quality rapidly worsens when evaluated on vectors outside geodesic interpolation lines between pairs of latent vectors. In other words, the manifold on which the trained decoder can produce plausible images can be described as a complete graph, heterogeneously distributed on the surface of the unit n-sphere.

Instead of inverting GLO, our method cGLO uses a reparameterization of the IIP, like DIP [41], to benefit from the structural bias of the convolutional decoder. However, the objective function described in Eq. (2), is cast into the framework of GLO [46], detailed in Eq. (4).

At examination time, without prior training, the K slices $\bar{X} = \{\bar{x}_1, \dots, \bar{x}_K\}$ from one or several patients are re-constructed together such that the parameters θ , and the latent unit vectors $\bar{Z} = \{\bar{z}_1, \dots, \bar{z}_K\}$ are jointly learned through:

$$\bar{Z}^*, \theta^* = \arg \min_{\bar{Z}, \theta} \frac{1}{K} \sum_{i=1}^K \|\mathcal{T}_{\phi_e} \circ f_{\theta}(\bar{z}_i) - y_{i, \phi_e}\|_2^2 \quad s.t. \quad \|\bar{z}_i\|_2 = 1 \quad (5)$$

$$\bar{X}^* = f_{\theta^*}(\bar{Z}^*) \quad (6)$$

where \mathcal{T}_{ϕ_e} is the Radon transform sampled on experimental viewing angles ϕ_e and y_{i, ϕ_e} are the experimental profiles obtained from slice \bar{x}_i . This method comes with two improvements: (i) it avoids the overfitting issue of DIP because of the shared decoder between the entire set of slices \bar{X}^* , given sufficient slices to reconstruct, and (ii) leads to better reconstructions as adding supplementary experimental profiles to the objective tends to stabilize the optimization process detailed in Eq. (5). Furthermore, the set of profiles can easily be augmented by linear interpolation along the vertical axis, i.e. the axis orthogonal to the slices plane. In this case, reconstructions are conducted using the entire augmented set, then reconstructions corresponding to interpolated measurements are discarded. The impact of the number of profiles, K , on performances is detailed in the ablation study in Appendix C.

Given availability of a training set of full-dose CT scans, i.e. a set of slices $X = \{x_1, \dots, x_N\}$, additional prior knowledge may be enforced by learning an appropriate initial set of parameters θ_0 , for the decoder f_{θ} , in an unsupervised manner following Eq. (3) and Eq. (4):

$$\theta_0 = \arg \min_{Z, \theta} \frac{1}{N} \sum_{i=1}^N \|f_{\theta}(z_i) - x_i\|_2^2 \quad s.t. \quad \|z_i\|_2 = 1 \quad (7)$$

It is expected for the set of parameters θ_0 to be closer to θ^* than random weights, thus easing the optimization of Eq. (5), especially when ϕ_e is very sparse. The latent vectors from Eq. (7) are not reused so that the set \bar{Z} of Eq. (5) is always randomly initialized.

3 Experiments

Experiments have been conducted on two commonly used datasets which are publicly available on The Cancer Imaging Archive (TCIA) platform [53]. The methods involved in these experiments are: (a) cGLO, FBP [1] and DIP [45] *without* training data, and (b) cGLO, cSGM [25] and MCG [26] *with* training sub-datasets of varying sizes. Sub-datasets are limited to 35% portions of the initial datasets because the tested methods did not achieve significant performance gain above this threshold. All the methods are compared with the same numbers of experimental viewing angles: 9, 23 and 50. The DPS method [23] is omitted as it is equivalent to MCG for experiments conducted in this work, i.e. full-dose sparse CT. Implementation details concerning our decoder network architecture and hyperparameter values for each method are provided at the end of the section.

3.1 Datasets

The Lung Image Database Consortium (LIDC) [54] image collection was collected using lung cancer screenings from 1018 patients. It consists of thoracic CT scans completed with radiologists annotations for nodule segmentation. The Low-dose CT image and projection dataset (LDCT) [55] is comprised of 299 CT scans of patient heads, chests and abdomens and their respective (full) clinical doses. In addition, the LDCT dataset also includes simulated reduced doses, by Poisson noise insertion, and the location and diagnosis for positive findings. In the presented experiments, only CT scan slices from both datasets are used. Depending on the optimization process, slices are either directly compared using a pixel-wise metric, or indirectly via simulated measurements obtained from the application of the same forward operator, i.e. a full dose parallel-beam geometry with viewing angles equally distributed across 180 degrees. Similarly to Song et al. [25] and Chung et al. [26], our approach treats every slice independently. Therefore, though 3D scan geometric parameters such as pixel spacing and slice thickness may vary across patients, slices are not resampled, such that 3D volumes can have different number of slices and spatial scales. The native resolution of slices is 512×512 pixels for both datasets, but the LIDC slices are downsized to a resolution of 320×320 pixels. For experiments to be representative of various realistic situations with sparse or abundant data, training sub-datasets consisting of portions of the LIDC and LDCT collections are prepared. Details of such datasets are given in table 1. The LIDC and the LDCT test sets consist of five scans respectively totaling 791 and 1089 slices. Regarding experiments involving training sub-datasets, Peak Signal to Noise Ratio (PSNR) and Structural SIMilarity (SSIM) metrics are estimated on the total test set where each 3D volume is reconstructed independently, meaning that five independent reconstructions are computed. However, experiments conducted with cGLO and DIP, without any training datasets, are tested on a restricted set of 100

slices from 1 patient due to the computational time of the DIP approach. For these latter experiments, reconstructions computed with FBP and associated quantitative metrics are added as a baseline.

Portion	# of scans	# of slices	Portion	# of scans	# of slices
35%	350	65 033	35%	103	16 924
10%	100	17 898	10%	29	4 989
2%	20	2 906	2%	6	930

(a) LIDC sub-datasets

(b) LDCT sub-datasets

Table 1: Sub-datasets used for training with their corresponding number of 3D scans and slices. 3D scans are always fully included.

3.2 Implementation details

In the presented experiments, the geometry of the decoder’s latent space is set to the unit n-sphere, similarly to state-of-the-art representation learning approaches [46]. The latent space dimension is set to 320 for experiments on the LIDC dataset and 512 for the LDCT dataset. Being a reference in the literature of generative models, the Deep Convolutional Generative Adversarial Network (DCGAN) [50] architecture is used for the decoder. As illustrated in figure 1, the latent code firstly goes through a linear block and is mapped to a feature map of shape $2 \times 2 \times C$, with C the desired number of channels for the first convolutional layer. From layer to layer the input is upsampled by a factor of 2 (last layer upscale factor may vary to fit the desired output image resolution) and the number of channels is cut by half. Hence, the image resolution, the latent dimension and C completely define the structure of the decoder. The number of input channels C is set to 8192 for both experiments on the LIDC and the LDCT sub-datasets.

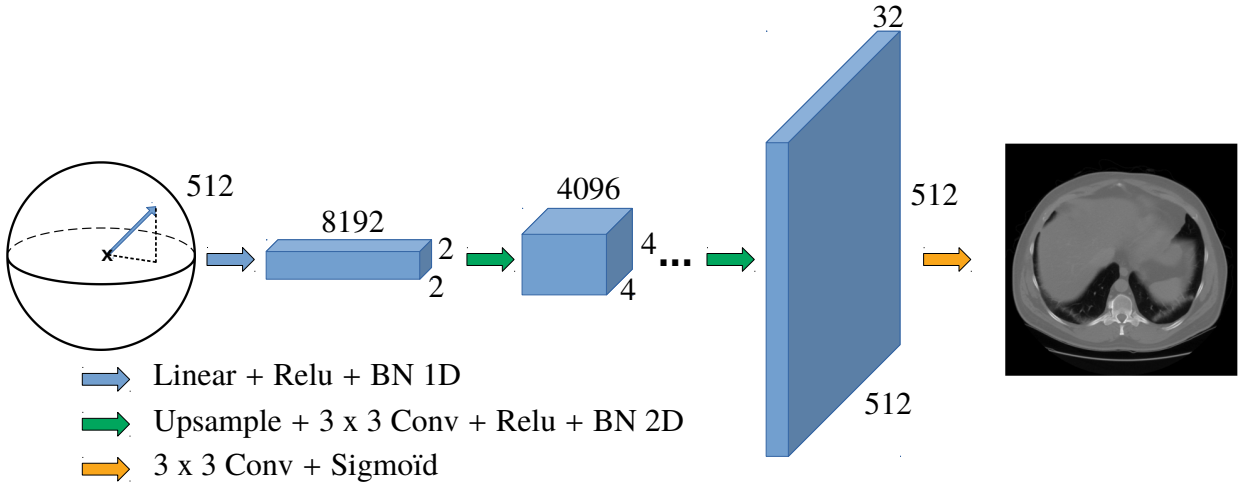


Figure 1: Generator DCGAN-like architecture, latent dimension (512) and final resolution (512×512) corresponding to the LDCT sub-datasets experiments.

cGLO optimizations are conducted with the Adam algorithm [56]. The learning rates for the latent codes and the decoder weights are both set to 10^{-3} while training on CT reconstruction, i.e. the step described in Eq. (7), and respectively set to 10^{-2} and 10^{-4} when reconstructing from experimental measurements, i.e. the step detailed in Eq. (5). Although learning rates are kept constant, batch sizes are increased along specified schedules. It leads to faster training and is statistically equivalent to decreasing learning rates [57]. Measurements are augmented by a factor of 8 for reconstructions involving parameters initialization with training set and by factors (8, 16 and 16) for angles (9, 23 and 50) when no training data is used.

DIP, cSGM and MCG hyper-parameters, model architecture, and other implementation details are set to what is respectively provided by Baguer et al. [45], Song et al. [25] and Chung et al. [26] for their sparse-view CT experiments. The DIP network is initialized as described in Eq. (3) on a reconstruction computed with FBP.

4 Results and discussion

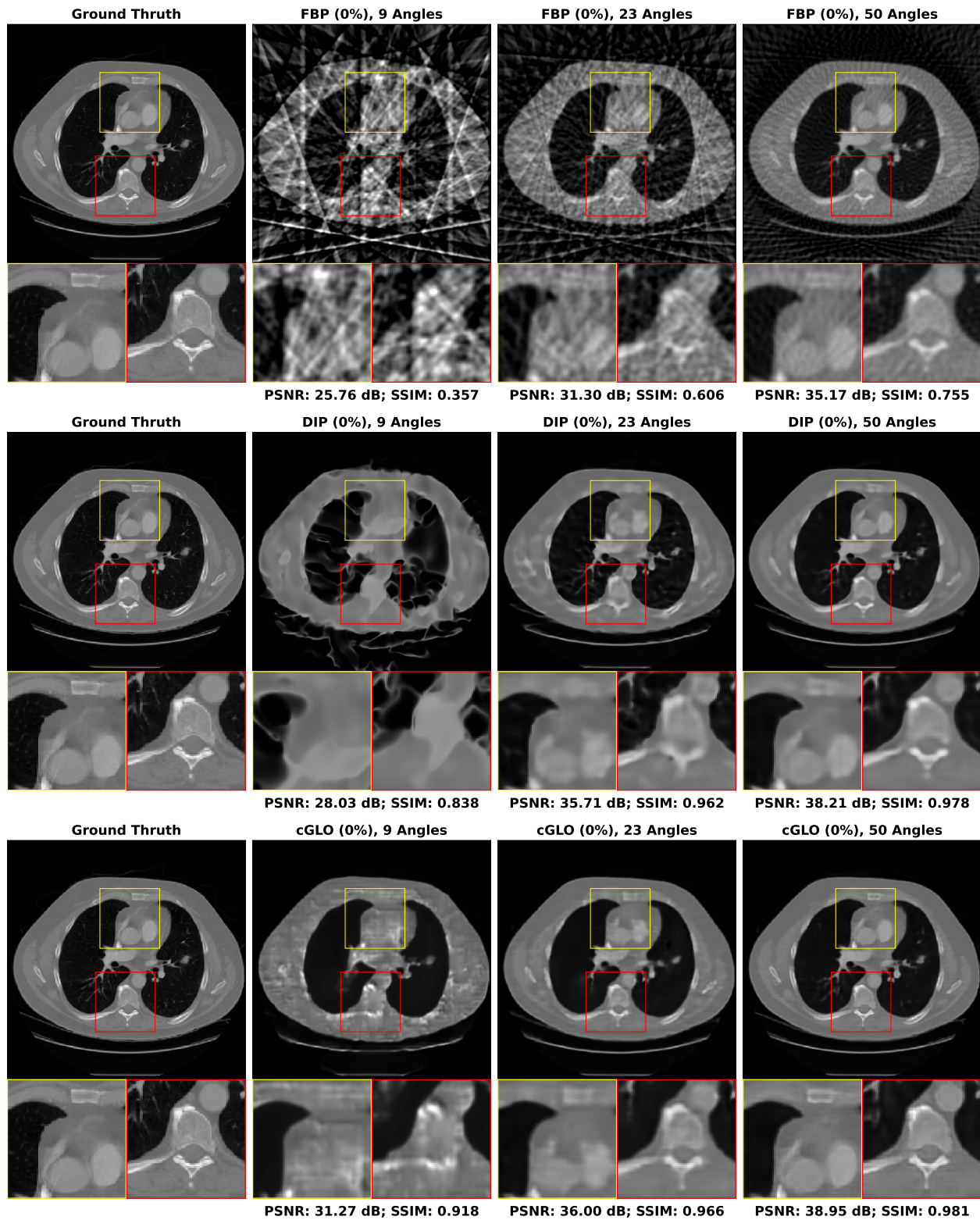


Figure 2: Examples of reconstructions given 9, 23 and 50 experimental viewing angles, obtained with FBP (upper row), DIP (middle row) and cGLO (lower row). Reconstructions are achieved without prior unsupervised training.

In this section, our method cGLO is compared with DIP and the conventional baseline FBP for reconstructions obtained *without* any training dataset. Regarding this specific use case, DIP currently holds state-of-the-art performance. These approaches are evaluated using quantitative pixel-wise (PSNR) and structural (SSIM) metrics which are detailed in Table 2, alongside qualitative results consisting of examples of reconstructions from the LIDC test set and given in figure 2. Our method is also tested against cSGM and MCG on use cases *with* available training datasets of varying sizes. To the best of our knowledge, with prior unsupervised training, MCG achieves state-of-the-art reconstruction quality for sparse CT. Quantitative metrics for 9, 23, and 50 experimental viewing angles are given in figure 3 and detailed in Appendix D. Qualitative results consist of examples of reconstructions from cGLO, cSGM and MCG trained on the smallest sub-dataset, i.e. a 2% portion of the LIDC dataset. These reconstructions are presented in figure 4. Additional examples, for experimental setups corresponding to different combinations of training dataset sizes and number of viewing angles are provided in Appendix E.

4.1 Without prior unsupervised training

As shown in Table 2, on the use case with no training dataset available, our method cGLO outperforms DIP and FBP reconstruction methods for every set of experimental viewing angles, regarding both PSNR and SSIM metrics. Most notably given 9 experimental viewing angles, cGLO offers a PSNR gain of +3.15 dB on the LIDC test set compared to DIP.

Method	Angles	LIDC 320×320		LDCT 512×512	
		PSNR ↑	SSIM ↑	PSNR ↑	SSIM ↑
FBP	9	25.99 ±0.11	0.366 ±0.011	26.31 ±0.09	0.454 ±0.006
DIP	9	<u>28.26</u> ±0.32	<u>0.843</u> ±0.009	27.78 ±0.39	<u>0.842</u> ±0.010
cGLO	9	31.41 ±0.34	0.916 ±0.005	30.28 ±0.29	0.906 ±0.003
FBP	23	31.46 ±0.19	0.605 ±0.004	30.79 ±0.08	0.623 ±0.004
DIP	23	<u>35.50</u> ±0.23	<u>0.954</u> ±0.002	33.64 ±0.41	<u>0.935</u> ±0.005
cGLO	23	36.18 ±0.39	0.966 ±0.002	35.99 ±0.64	0.956 ±0.005
FBP	50	35.31 ±0.56	0.763 ±0.005	33.11 ±0.10	0.724 ±0.002
DIP	50	<u>37.40</u> ±0.36	<u>0.973</u> ±0.002	36.36 ±0.31	<u>0.960</u> ±0.002
cGLO	50	38.92 ±0.27	0.980 ±0.001	38.75 ±0.20	0.973 ±0.001

Table 2: PSNR and SSIM median ± half Inter Quartile Range (IQR) values for reconstructions of 100 slices from the LIDC and the LDCT test datasets given 9, 23 and 50 experimental viewing angles. Best and second best results are respectively indicated as bold and underline for each angle and metric.

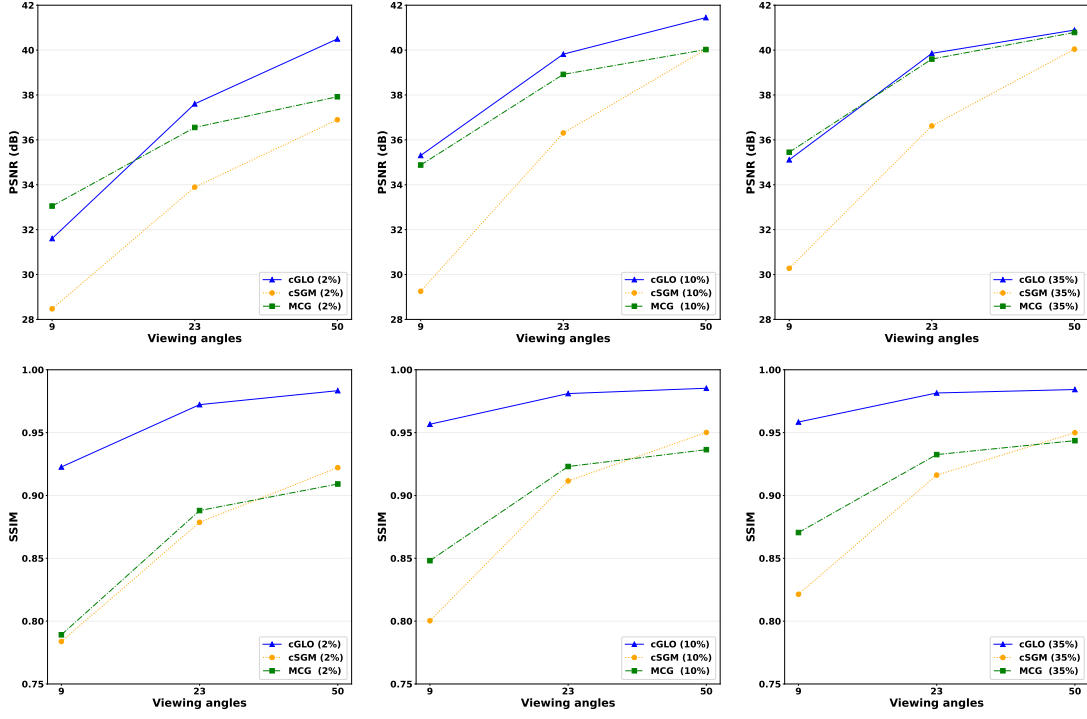
Also, median PSNR and SSIM values reported in Table 2 indicate that the performance gap, at the advantage of cGLO over DIP, increases as the set of experimental viewing angles gets smaller. More specifically, the PSNR gap between cGLO and DIP more than double between experiments involving 50 (+1.52 dB) and 9 (+3.15 dB) viewing angles on the LIDC test set. In other words, our method is more robust for solving increasingly sparse CT with no prior training when compared to DIP.

It can also be observed in figure 2 on the reconstruction example given 9 experimental viewing angles that, contrary to cGLO, DIP reproduces some of the deformations induced by the strong artifacts from FBP. This corroborates the larger difference between cGLO and DIP regarding SSIM metric for this experiment (+0.073). It is a direct effect of DIP network parameters first being initialized on the FBP reconstruction. However, by skipping this initialization step, DIP reconstructions and quantitative performances would be further degraded.

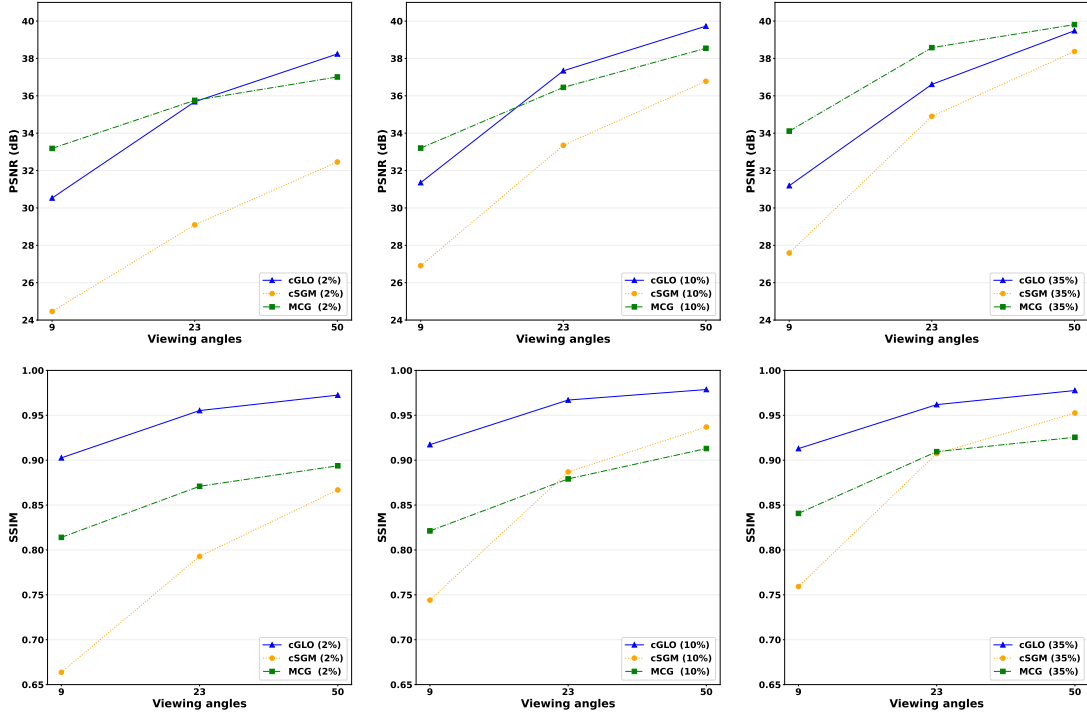
4.2 With prior unsupervised training

Quantitative performance

As presented in figure 3, cGLO outperforms cSGM for all data and viewing angles configurations regarding both median PSNR and SSIM values. The largest performance gaps are observed for experiments given 9 viewing angles, with PSNRs ranging between +3.13 dB and +6.06 dB respectively for the 2% and 10% LIDC training sub-dataset. In addition, median PSNR and especially median SSIM curves in figure 3 show an increasing advantage of cGLO over cSGM as the set of experimental viewing angles gets sparser and/or the training dataset gets smaller. Specifically for LIDC experiments, the lead in favor of cGLO over cSGM regarding SSIM starts at +0.034 (2% sub-dataset and 9 viewing angles) to reach +0.139 (35% sub-dataset and 50 viewing angles). Furthermore, cGLO achieves higher median SSIM metrics values in all experimental setups, even in abundant data configurations with large training sub-datasets



(a) PSNR and SSIM - LIDC dataset



(b) PSNR and SSIM - LDCT dataset

Figure 3: PSNR and SSIM median values curves corresponding to reconstructions of slices from the LIDC (a) and the LDCT (b) test sets given 9, 23 and 50 experimental viewing angles. Each column is associated with one of the 2%, 10% and 35% training sub-datasets presented in table 1.

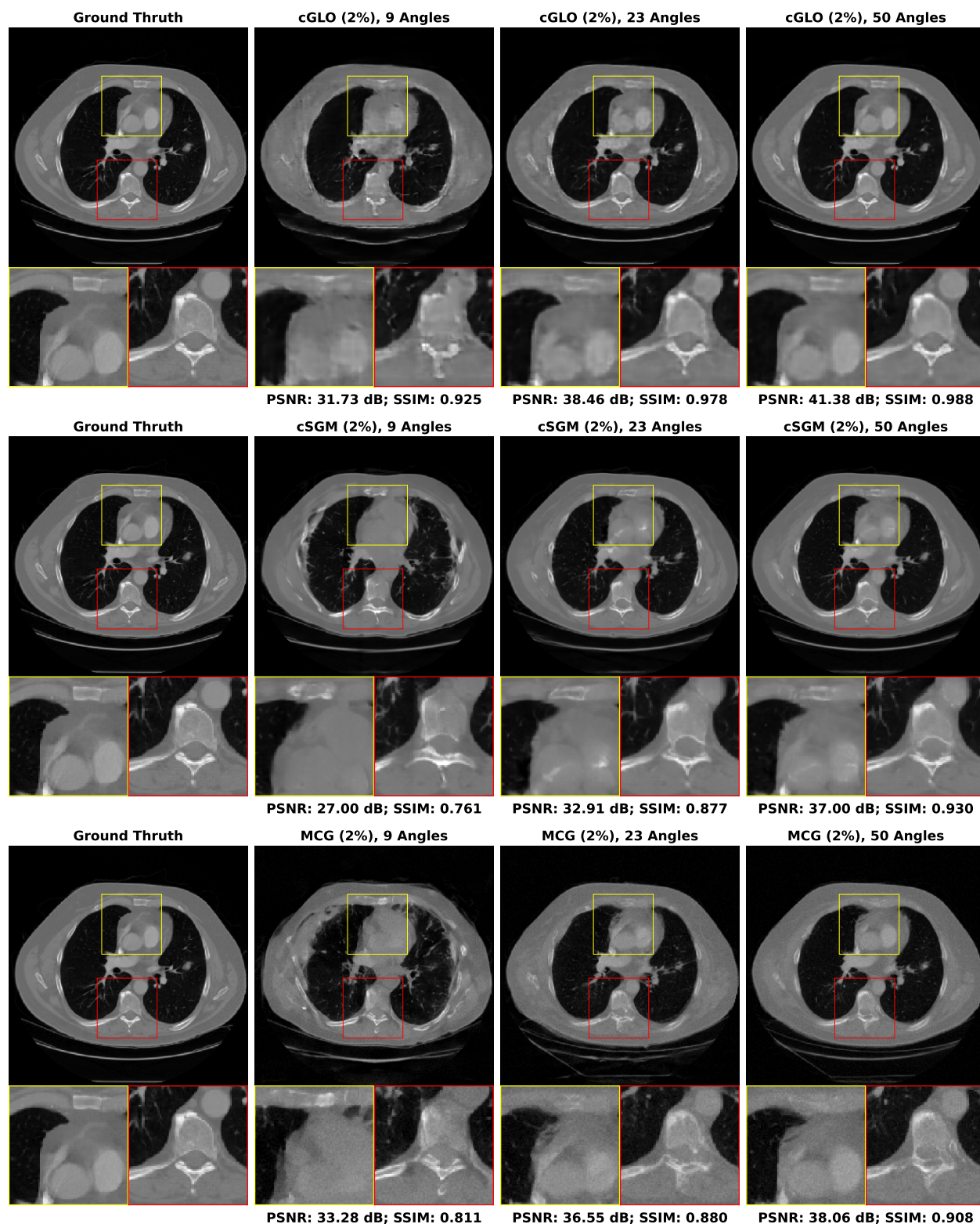


Figure 4: Examples of reconstructions given 9, 23 and 50 experimental viewing angles, obtained with cGLO (upper row), cSGM (middle row) and MCG (lower row). Methods are trained on the sub-dataset consisting of a 2% portion of the LIDC dataset.

and many experimental viewing angles when compared to both cSGM and MCG. When compared to MCG on the same configurations as above, cGLO demonstrates a SSIM gain ranging from +0.041 to +0.134. Figure 3 also displays a dominance of MCG over cGLO regarding PSNR metrics on use cases with abundant data, e.g. with prior training on the 35% LDCT sub-dataset with a superiority of +0.33 dB, +1.97 dB and +2.92 dB for PSNRs given respectively 50, 23 and 9 viewing angles. On the smaller 2% and 10% training sub-datasets, cGLO equals or outperforms MCG regarding PSNR given experimental setups with more than 23 viewing angles. For instance on the LIDC experiments, a gain rising from +0.9 dB (10% sub-dataset and 23 viewing angles) to +2.58 dB (2% sub-dataset and 50 viewing angles) can be observed.

The effects of training dataset sizes and viewing angles are consistent between experiments but are especially visible on the curves describing SSIM metrics for reconstructions from the LDCT test set in last row of panels of figure 3. Considering one method (one color), higher vertical gaps between panels of the same row show greater dependency on training dataset sizes, while steeper slopes within each panel indicate a superior impact of viewing angles on performance. In this regard, cSGM is the most affected by a diminishing number of viewing angles and/or smaller training datasets. For example, when considering configurations with abundant data, e.g. the LIDC 35% sub-dataset, cSGM PSNR values plummet from 40.04 dB to 30.28 dB implying a -9.76 dB decrease between 50 and 9 viewing angles. As intended by its design, MCG demonstrates in the same context the most robustness (specifically regarding PSNRs) against sparser experimental setups with a -5.34 dB loss. cGLO sustains performances close to MCG with a -5.78 dB drop. Finally, our method is the most parsimonious/robust concerning training dataset sizes. Indeed, in the configuration with abundant viewing angles (50), cGLO PSNRs for LIDC experiments fall from 40.89 dB to 40.50 dB, i.e. a small loss of -0.39 dB when compared to MCG (-2.87 dB) and cSGM (-3.14 dB).

The prominent points of the quantitative performances comparison between cGLO, cSGM and MCG are the following. For every configurations, cGLO offers better reconstructions than cSGM and MCG regarding the SSIM metric and also surpasses cSGM when considering PSNR values. Further cGLO is less dependent on training dataset sizes than MCG which is more robust to reduced viewing angles. Consequently, when comparing PSNR values, cGLO provides better performances than MCG in scenarios with more than 23 angles and restricted access to training data, e.g. less than 10% of the LIDC dataset.

Effect of large training datasets on cGLO

As illustrated in figure 3, contrary to cSGM and MCG, as the training datasets becomes larger, cGLO PSNR performances stagnate and even slightly worsen. More specifically for PSNRs, averaged over angle configurations, a drop is observed when cGLO is trained on the 35% rather than the 10% sub-dataset, from 38.86 dB to 38.62 dB for LIDC, and from 36.14 dB to 35.74 dB for LDCT. Given a fixed representation capacity for our decoder architecture, i.e. a fixed number of input channels C , the model becomes under-parameterized after a given training dataset size is reached. Since the model parameters and the latent codes are jointly optimized in Eq. (7) with respect to a data-likelihood objective function, the model error distribution is widely spread over the entire training dataset [52]. Consequently, when the data variability overcomes the model capacity, each additional training example further deteriorates the average prediction quality. Ideally, the model capacity should be tuned to best fit each experimental setup. However, the experiments realized in this paper demonstrate that even with a fixed decoder architecture, cGLO produces superior reconstructions for multiple experimental setups.

Reconstruction structural quality

Figure 4 compares reconstructions computed with cGLO, cSGM and MCG from the LIDC test dataset. Reconstruction quality clearly degrades as the number of experimental viewing angles diminishes. The type of degradation, however, differs between cGLO and the score-based methods cSGM and MCG. While cGLO reconstructions lack sharp details and get noisier for very sparse CT or when trained on very small datasets, cSGM and MCG tend to alter the structural integrity of the slices. This observation corroborates and explains the total dominance of cGLO over all the methods when comparing median SSIM curves rather than median PSNR curves in figure 3.

The fact that cSGM/MCG and cGLO yield different reconstruction structures for more difficult experimental setups can be explained by the way each model employs experimental data. cSGM uses a proximal optimization step to mix experimental data with unconditioned samples. Details are provided in Appendix B (Eq. (16)). This leads to a cost function expressing a balance between data likelihood and prior, which only enforces a loose constraint on the conformity of the proposed reconstruction to experimental data. When the number of viewing angles diminishes, there are increasing structural deformations as shown in figure 4. MCG correction step (detailed in Appendix B Eq. (20)) prevents the inference mechanism to deviate from data consistency for sparse experimental setups. However, when trained on insufficient data quantities, the assumption that the score-model approximate the data manifold may not hold anymore. On the contrary, the cost function of cGLO, described in equation (5), enforces a strict constraint on

experimental data. With decreasing viewing angles, the energy landscape of this cost function becomes less smooth, leading to the presence of local minima and harder convergence of the optimization process. As seen in figure 4, this leads to degraded reconstructions with more noise and less details at 9 viewing angles for example. However, contrary to cSGM and MCG, cGLO does not tend to create hallucinated structures.

5 Conclusion

In this work we presented cGLO, a novel unsupervised method to solve IIPs built upon the general framework of GLO [46]. Contrary to supervised strategies, our method does not require a fixed experimental setup. Analogously to DIP [45], our strategy benefits from the structural prior induced by convolutional decoders without any preceding training. Furthermore, cGLO takes advantage of a shared objective function by reconstructing multiple slices simultaneously at examination time and may be initialized beforehand on an unsupervised training dataset of any size to improve reconstruction quality. In other words, our approach is a very flexible plug-and-play reconstruction technique that can be used *with or without* unsupervised training data and *without* any assumption on the IIP at hand.

cGLO was tested on full-dose sparse view CT which is a widely studied reconstruction problem arising in medical imaging and compared to the current state-of-the-art approaches, MCG [26] for unsupervised cases and DIP for cases with no prior training. Experiments conducted in this paper cover a wide range of realistic setups with varying amount of available training data and experimental viewing angles. Quantitative results regarding pixel-wise metric (PSNR) demonstrate that cGLO is a parsimonious and robust reconstruction method as it offers similar to better performances when compared to MCG on small data regimes with sufficient viewing angles and surpasses DIP in every experimental setups. Moreover, for the entire set of conducted experiments, cGLO offers the best performances with respect to the structural metric (SSIM). Indeed, reconstruction examples illustrate that cGLO exhibits a propensity to preserve the structural integrity of reconstructions and it avoids the inclusion of hallucinated pattern, even for very ill-posed IIPs, thanks to its straightforward conditioning to experimental measurements.

While the performance of cGLO has been tested on a tomographic reconstruction problem, the framework developed in this article can be readily applied to other ill-posed IIPs, such as MRI reconstruction from a sparsely sampled k-space. Furthermore, since the cGLO approach only requires the knowledge of the forward operator, it could be extended to solve non-linear IIPs. One of the main interests of cGLO is that it does not require any backward operator, such as FBP for tomographic reconstruction. Consequently, it is a method of choice for IIPs where such operators do not exist, such as multi-material CT reconstruction. Future work will explore the application of cGLO to such IIPs. Since cGLO efficiently learns correlations between the output channels of its decoder network, further developments will also focus on multi-task applications, such as jointly learning reconstruction and segmentation.

References

- [1] Stanley R. Deans. *The Radon transform and some of its applications*. Wiley, 1983.
- [2] Haoyu Wei, Florian Schiffers, Tobias Würfl, Daming Shen, Daniel Kim, Aggelos Katsaggelos, and Oliver Cossairt. 2-Step Sparse-View CT Reconstruction with a Domain-Specific Perceptual Network 2020. arXiv:2012.04743 [eess.IV].
- [3] Jonas Adler and Ozan Öktem. Deep Bayesian Inversion. 2018. arXiv:1811.05910 [stat.ML].
- [4] Jonas Adler and Ozan Öktem. Learned Primal-Dual Reconstruction. *IEEE Transactions on Medical Imaging*, 37(6):1322–1332, 2018. doi: 10.1109/TMI.2018.2799231.
- [5] Hoyeon Lee, Jongha Lee, Hyeongseok Kim, Byungchul Cho, and Seungryong Cho. Deep-Neural-Network-Based Sinogram Synthesis for Sparse-View CT Image Reconstruction. *IEEE Transactions on Radiation and Plasma Medical Sciences*, 3(2):109–119, 2019. doi: 10.1109/TRPMS.2018.2867611.
- [6] Bo Zhu, Jeremiah Z. Liu, Stephen F. Cauley, Bruce R. Rosen, and Matthew S. Rosen. Image reconstruction by domain-transform manifold learning. *Nature*, 555(7697):487–492, 2018. doi: 10.1038/nature25988.
- [7] Francesco Tonolini, Jack Radford, Alex Turpin, Daniele Faccio, and Roderick Murray-Smith. Variational inference for computational imaging inverse problems. *Journal of Machine Learning Research*, 21(1):7285–7330, 2020. arXiv:1904.06264 [cs.LG].
- [8] Jonas Adler and Ozan Öktem. Solving ill-posed inverse problems using iterative deep neural networks. *Inverse Problems*, 33(12):124007, 2017. doi: 10.1088/1361-6420/aa9581.
- [9] Ian Goodfellow, Jean Pouget-Abadie, Mehdi Mirza, Bing Xu, David Warde-Farley, Sherjil Ozair, Aaron Courville, and Yoshua Bengio. Generative adversarial networks. In *Advances in Neural Information Processing Systems*, 2014. arXiv:1406.2661 [stat.ML].
- [10] Weihao Xia, Yulun Zhang, Yujiu Yang, Jing-Hao Xue, Bolei Zhou, and Ming-Hsuan Yang. GAN Inversion: A Survey. *IEEE Transactions on Pattern Analysis and Machine Intelligence*, 45(3):3121–3138, 2023. doi: 10.1109/TPAMI.2022.3181070.
- [11] Yang Song and Stefano Ermon. Generative Modeling by Estimating Gradients of the Data Distribution. In *Advances in Neural Information Processing Systems*, 2019. arXiv:1907.05600 [cs.LG].
- [12] Jonathan Ho, Ajay Jain, and Pieter Abbeel. Denoising Diffusion Probabilistic Models. In *Advances in Neural Information Processing Systems*, 2020. arXiv:2006.11239 [cs.LG].
- [13] Prafulla Dhariwal and Alexander Quinn Nichol. Diffusion Models beat GANs on Image Synthesis In *Advances in Neural Information Processing Systems*, 2021. arXiv:2115.05233 [cs.LG].
- [14] Gwanghyun Kim, Taesung Kwon, and Jong Chul Ye. Diffusion-CLIP: Text-Guided Diffusion Models for Robust Image Manipulation In *Computer Vision and Pattern Recognition*, 2022. arXiv:2110.02711 [cs.CV].
- [15] Robin Rombach, Andreas Blattman, Dominik Lorenz, Patrick Esser, and Björn Ommer. High-Resolution Image Synthesis with Latent Diffusion Models Manipulation In *Computer Vision and Pattern Recognition*, 2022. arXiv:2112.10752 [cs.CV].
- [16] Yang Song, Prafulla Dhariwal, Mark Chen, and Ilya Sutskever. Consistency Models. 2023. arXiv:2303.01469 [cs.LG].
- [17] Yang Song, Jascha Sohl-Dickstein, Diederik P. Kingma, Abhishek Kumar, Stefano Ermon, and Ben Poole. Score-Based Generative Modeling through Stochastic Differential Equations. In *International Conference on Learning Representations*, 2021. arXiv:2011.13456 [cs.LG].
- [18] Alexander Quinn Nichol and Prafulla Dhariwal. Improved Denoising Diffusion Probabilistic Models. In *International Conference on Machine Learning*, 2021. arXiv:2102.09672 [cs.LG].
- [19] Yang Song and Stefano Ermon. Improved Techniques for Training Score-Based Generative Models. In *Advances in Neural Information Processing Systems*, 2020. arXiv:2006.09011 [cs.LG].
- [20] Hyungjin Chung, Byeongsu Sim, and Jong Chul Ye. Come-Closer-Diffuse-Faster: Accelerating Conditional Diffusion Models for Inverse Problems through Stochastic Contraction In *Computer Vision and Pattern Recognition*, 2021. arXiv:2112.05146 [eess.IV].
- [21] Andreas Lugmayr, Martin Danelljan, Andres Romero, Fisher Yu, Radu Timofte, and Luc Van Gool. RePaint: Inpainting Using Denoising Diffusion Probabilistic Models. In *Computer Vision and Pattern Recognition*, 2022. doi: 10.1109/CVPR52688.2022.01117.

- [22] Hyungjin Chung, Jeongsol Kim, Sehui Kim, and Jong Chul Ye. Parallel Diffusion Models of Operator and Image for Blinf Inverse Problems In *Computer Vision and Pattern Recognition*, 2023. arXiv:2211.10656 [cs.CV].
- [23] Hyungjin Chung, Jeongsol Kim, Michael T. Mccann, Marc L. Klasky, and Jong Chul Ye. Diffusion Posterior Sampling for General Noisy Inverse Problems arXiv:2209.14687 [stats.ML].
- [24] Jiaming Liu, Rushil Anirudh, Jayaraman J. Thiagarajan, Stewart He, Aditya Mohan, Ulugbek S. Kamilov, and Hyojin Kim. DOLCE: A Model-Based Probabilistic Diffusion Framework for Limited-Angle CT Reconstruction In *International Conference on Computer Vision*, 2023. arXiv:2211.12340 [eess.IV].
- [25] Yang Song, Liyue Shen, Lei Xing, and Stefano Ermon. Solving Inverse Problems in Medical Imaging with Score-Based Generative Models. In *International Conference on Learning Representations*, 2022. arXiv:2111.08005 [eess.IV].
- [26] Hyungjin Chung, Byeongsu Sim, Dohoon Ryu, and Jong Chul Ye. Improving Diffusion Models for Inverse Problems using Manifold Constraints In *Advances in Neural Information Processing Systems*, 2022. arXiv:2206.00941 [cs.LG].
- [27] Elad Richardson, Yuval Alaluf, Or Patashnik, Yotam Nitzan, Yaniv Azar, Stav Shapiro, and Daniel Cohen-Or. Encoding in Style: A StyleGAN Encoder for Image-to-Image Translation. In *Computer Vision and Pattern Recognition*, 2021. doi: 10.1109/CVPR46437.2021.00232.
- [28] Guim Perarnau, Joost van de Weijer, Bogdan Raducanu, and Jose M. Àlvarez. Invertible Conditional GANs for image editing. 2016. arXiv:1611.06355 [cs.CV].
- [29] Rameen Abdal, Yipeng Qin, and Peter Wonka. Image2StyleGAN: How to Embed Images Into the StyleGAN Latent Space? In *International Conference on Computer Vision*, 2019. arXiv:1904.03189 [cs.CV].
- [30] Minyoung Huh, Richard Zhang, Jun-Yan Zhu, Sylvain Paris, and Aaron Hertzmann. Transforming and Projecting Images into Class-Conditional Generative Networks. In *European Conference on Computer Vision*, 2020. doi: 10.1007/978-3-030-58536-5_2.
- [31] Jun-Yan Zhu, Philipp Krähenbühl, Eli Shechtman, and Alexei A. Efros. Generative Visual Manipulation on the Natural Image Manifold. In *European Conference on Computer Vision*, 2016. doi: 10.1007/978-3-319-46454-1_36.
- [32] Jiapeng Zhu, Yujun Shen, Deli Zhao, and Bolei Zhou. In-Domain GAN Inversion for Real Image Editing. In *European Conference on Computer Vision*, 2020. doi: 10.1007/978-3-030-58520-4_35.
- [33] David Bau, Jun-Yan Zhu, Jonas Wulff, William Peebles, Hendrik Strobelt, Bolei Zhou, and Antonio Torralba. Seeing What a GAN Cannot Generate. In *International Conference on Computer Vision*, 2019. arXiv:1910.11626 [cs.CV].
- [34] Jeff Donahue, Philipp Krähenbühl, and Trevor Darrell. Adversarial Feature Learning. In *International Conference on Learning Representations*, 2017. arXiv:1605.09782 [cs.LG].
- [35] Vincent Dumoulin, Ishmael Belghazi, Ben Poole, Olivier Mastropietro, Alex Lamb, Martin Arjovsky, and Aaron Courville. Adversarially Learned Inference. In *International Conference on Learning Representations*, 2017. arXiv:1606.00704 [stat.ML].
- [36] Jiapeng Zhu, Deli Zhao, Bo Zhang, and Bolei Zhou. Disentangled Inference for GANs With Latently Invertible Autoencoder. *International Journal of Computer Vision*, 130(5):1259–1276, 2022. doi: 10.1007/s11263-022-01598-5.
- [37] Giannis Daras, Joseph Dean, Ajil Jalal, and Alexandros G. Dimakis. Intermediate Layer Optimization for Inverse Problems using Deep Generative Models. 2021. arXiv:2102.07364 [cs.LG].
- [38] Dmitry Ulyanov, Andrea Vedaldi, and Victor Lempitsky. It Takes (Only) Two: Adversarial Generator-Encoder Networks. In *AAAI Conference on Artificial Intelligence*, 2018. doi: 10.1609/aaai.v32i1.11449.
- [39] Varun A. Kelkar and Mark Anastasio. Prior Image-Constrained Reconstruction using Style-Based Generative Models. In *International Conference on Machine Learning*, 2021. arXiv:2102.12525 [eess.IV].
- [40] Sachit Menon, Alexandru Damian, Shijia Hu, Nikhil Ravi, and Cynthia Rudin. PULSE: Self-Supervised Photo Upsampling via Latent Space Exploration of Generative Models. In *Computer Vision and Pattern Recognition*, 2020. doi: 10.1109/CVPR42600.2020.00251.
- [41] Dmitry Ulyanov, Andrea Vedaldi, and Victor Lempitsky. Deep Image Prior. In *Computer Vision and Pattern Recognition*, 2018. arXiv:1711.10925 [cs.CV].
- [42] Olaf Ronneberger, Philipp Fischer, and Thomas Brox. U-Net: Convolutional Networks for Biomedical Image Segmentation. In *Medical Image Computing and Computer-Assisted Intervention*, 2015. doi: 10.1007/978-3-319-24574-4_28.

- [43] Reinhard Heckel and Mahdi Soltanolkotabi. Denoising and Regularization via Exploiting the Structural Bias of Convolutional Generators. 2020. arXiv:1910.14634 [cs.LG].
- [44] Prithvijit Chakrabarty and Subhransu Maji. The Spectral Bias of the Deep Image Prior. 2019. arXiv:1912.08905 [cs.CV].
- [45] Daniel Otero Bague, Johannes Leuschner, and Maximilian Schmidt. Computed tomography reconstruction using deep image prior and learned reconstruction methods. *Inverse Problems*, 36(9):094004, 2020. doi: 10.1088/1361-6420/aba415.
- [46] Piotr Bojanowski, Armand Joulin, David Lopez-Paz, and Arthur Szlam. Optimizing the Latent Space of Generative Networks. In *International Conference on Machine Learning*, 2018. arXiv:1707.05776 [stat.ML].
- [47] Idan Azuri and Daphna Weinshall. Generative Latent Implicit Conditional Optimization when Learning from Small Sample. In *International Conference on Pattern Recognition*, 2021. doi: 10.1109/ICPR48806.2021.9413259.
- [48] Yedid Hoshen, Ke Li, and Jitendra Malik. Non-Adversarial Image Synthesis With Generative Latent Nearest Neighbors. In *Computer Vision and Pattern Recognition*, 2019. doi: 10.1109/CVPR.2019.00596.
- [49] Bi Xiao and Xiaokang Yang. Optimizing Generative Adversarial Networks in Latent Space. In *International Conference on Intelligent Computing, Automation and Systems*, 2019. doi: 10.1109/ICICAS48597.2019.00020.
- [50] Alec Radford, Luke Metz, and Soumith Chintala. Unsupervised Representation Learning with Deep Convolutional Generative Adversarial Networks. In *International Conference on Learning Representations*, 2016. arXiv:1511.06434 [cs.LG].
- [51] Diederik P. Kingma and Max Welling. Auto-Encoding Variational Bayes. In *International Conference on Learning Representations*, 2014. arXiv:1312.6114 [stat.ML].
- [52] Lucas Theis, Aäron van den Oord, and Matthias Bethge. A note on the evaluation of generative models. In *International Conference on Learning Representations*, 2016. arXiv:1511.01844 [stat.ML].
- [53] Kenneth Clark, Bruce Vendt, Kirk Smith, John Freymann, Justin Kirby, Paul Koppel, Stephen Moore, Stanley Phillips, David Maffitt, Michael Pringle, Lawrence Tarbox, and Fred Prior. The Cancer Imaging Archive (TCIA): Maintaining and Operating a Public Information Repository. *Journal of Digital Imaging*, 26(6):1045–1057, 2013. doi: 10.1007/s10278-013-9622-7.
- [54] Samuel G. Armato III. The Lung Image Database Consortium (LIDC) and Image Database Resource Initiative (IDRI): A Completed Reference Database of Lung Nodules on CT Scans. *Medical Physics*, 38(2):915–931, 2011. doi: 10.1118/1.3528204.
- [55] Taylor R. Moen, Baiyu Chen, David R. Holmes III, Xinhui Duan, Zhicong Yu, Lifeng Yu, Shuai Leng, Joel G. Fletcher, and Cynthia H. McCollough. Low-dose CT image and projection dataset. *Medical Physics*, 48(2):902–911, 2021. doi: 10.1002/mp.14594.
- [56] Diederik P. Kingma and Jimmy Ba. Adam: A Method for Stochastic Optimization. In *International Conference on Learning Representations*, 2015. arXiv:1412.6980 [cs.LG].
- [57] Samuel L. Smith, Pieter-Jan Kindermans, Chris Ying, and Quoc V. Le. Don’t Decay the Learning Rate, Increase the Batch Size. In *International Conference on Learning Representations*, 2018. arXiv:1711.00489 [cs.LG].
- [58] Frank Natterer and Frank Wübbeling. *Mathematical Methods in Image Reconstruction*. Society for Industrial and Applied Mathematics, 2001. doi: 10.1137/1.9780898718324.
- [59] Amir Beck and Marc Teboulle. A Fast Iterative Shrinkage-Thresholding Algorithm for Linear Inverse Problems. *SIAM Journal on Imaging Sciences*, 2(1):183–202, 2009. doi: 10.1137/080716542.
- [60] Brian D. O. Anderson. Reverse-time diffusion equation models. *Stochastic Processes and their Applications*, 12(3):313–326, 1982. doi: 10.1016/0304-4149(82)90051-5.
- [61] Pascal Vincent. A Connection Between Score Matching and Denoising Autoencoders. *Neural Computation*, 23(7):1661–1674, 2011. doi: 10.1162/NECO_a_00142.
- [62] Herbert E. Robbins. An empirical bayes approach to statistics. In *Breakthroughs in statistics*, 1992.

Appendix A: Computed Tomography

Given a narrow beam of X-ray photons of energy $E \in [0, \varepsilon]$, with a normalized dose spectrum $S(E)$, tracing through a material m with homogeneous density distribution ρ_m , the beam intensity decreases in accord with the Beer-Lambert law:

$$\frac{I}{I_0} = \int_0^\varepsilon S(E) \exp \left[- \left(\frac{\mu_m}{\rho_m} \right)_E \rho_m L \right] dE \quad (8)$$

where I_0 and I are respectively the input and observed intensities, L is the beam path length and μ_m the linear attenuation coefficient of material m . The ratio $\left(\frac{\mu_m}{\rho_m} \right)_E$ corresponds to the mass attenuation of material m . Depending on the energy level E , this macroscopic attenuation is obtained by adding up the effect of several absorption and scattering mechanisms, e.g. Rayleigh and Compton scattering, photoelectric absorption or pair production.

In medical tomodensitometry, the quantity of interest is the heterogeneous density distribution reflecting the patient internals. However, further assumptions are made to recover this distribution from experimental measurements: bones and other tissues are reduced to one equivalent material with water mass attenuation and the X-ray beam is considered monoenergetic.

Now, by considering an horizontal plane section through the patient body, i.e. a slice x , and by moving the source and detector as indicated in figure 5, it is possible to obtain a profile y , on the detector axis p , for the viewing angle ϕ :

$$y(p, \phi) = -\log \left(\frac{I}{I_0} \right) = \int_L x ds \quad (9)$$

For continuous p and ϕ the profiles y may be identified with the two-dimensional Radon transform [1], also called the forward operator \mathcal{T} , of the slice x , such that $y = \mathcal{T}(x)$. However, in practical use cases, projection profiles are acquired for a set of incremental values $\Phi = \phi_1, \dots, \phi_N$, which constitutes a sampling of the Radon transform. Moreover, shot noise following a Poisson process τ usually appears in experimental profiles for lower doses. Resulting experimental measurements can then be described by:

$$y_\Phi = \mathcal{T}_\Phi(x) + \tau \quad (10)$$

Given a number of viewing angles close to the Nyquist sampling criterion [58], and sufficiently low noise, the inverse of the sampled Radon transform \mathcal{T}_Φ^\dagger can be computed with standard methods, e.g. FBP, to retrieve the slice density map without producing artifacts. By stacking several slices, the two-dimensional information may be converted to three-dimensional information.

In the case of insufficient viewing angles, e.g. sparse CT, or in presence of too much noise, e.g. low-dose CT, the inverse problem becomes ill-posed. It is classically solved using iterative optimization algorithm [59] using a *Maximum A Posteriori* (MAP) formulation of the problem:

$$x^* = \arg \min_x \|\mathcal{T}_\Phi(x) - y_\Phi\|_2^2 + \mathcal{R}(x) \quad (11)$$

where \mathcal{R} is a real valued function used to regularize the optimization process by injecting prior information on the desired output x^* . Most common operators encountered in the literature to model this information are $\|x\|_1$, $\|x\|_2$ and Total Variation (TV), $\text{TV}(x) = \|\nabla x\|_1$.

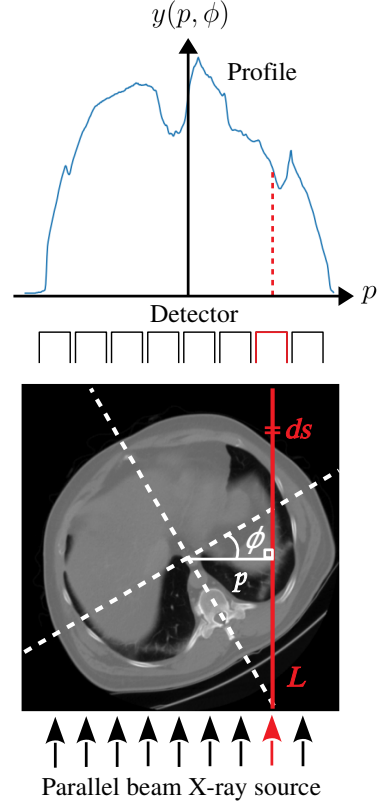


Figure 5: Parallel beam geometry profile acquisition for one viewing angle

Appendix B: Score-Based Generative Models (SGMs)

Unconditioned sampling with SGMs

The method developed by Song et al. [17] is generative. With a dataset of i.i.d. samples $\mathbf{x} \in X$ from an unknown distribution $p(\mathbf{x})$, it aims at generating new data samples. To this end, it defines a continuous diffusion process, that progressively perturbs samples from $p(\mathbf{x})$ into samples from a tractable prior distribution. It is formulated as a linear SDE as follows:

$$d\mathbf{x}_t = f(t)\mathbf{x}_t dt + g(t)d\mathbf{w}_t \quad (12)$$

where $t \in [0, 1]$, dt is an infinitesimal time step, f and g are real valued functions, \mathbf{w}_t is a standard Wiener process, and \mathbf{x}_t represents the samples through the perturbation process. The marginal probability distribution of \mathbf{x}_t , $p_t(\mathbf{x}_t)$ can be further derived from Eq. (12), as well as the transition distribution from \mathbf{x}_0 to \mathbf{x}_t , $p_{0t}(\mathbf{x}_t|\mathbf{x}_0)$. f and g are carefully designed so that, for any $p_0(\mathbf{x}) \equiv p(\mathbf{x})$, Eq. (12) ensures convergence at $t = 1$ towards a distribution $p_1(\mathbf{x})$ close to a Gaussian noise.

As demonstrated by Anderson [60], the reverse of the diffusion process, in Eq. (12), is also a diffusion process which can be written as the following reverse-time SDE:

$$d\mathbf{x}_t = [f(t)\mathbf{x}_t + g(t)^2 \nabla_{\mathbf{x}_t} \log p_t(\mathbf{x}_t)] dt + g(t) d\bar{\mathbf{w}}_t \quad (13)$$

where $\bar{\mathbf{w}}_t$ is a standard Wiener process in the reverse-time direction, and dt indicates an infinitesimal negative time step. Solving Eq. (13) from $t = 1$ to $t = 0$ corresponds to a continuous denoising, yielding data samples $\mathbf{x}_0 \sim p_0(\mathbf{x}) \equiv p(\mathbf{x})$ from noise samples [17]. However, it requires the score function $\nabla_{\mathbf{x}_t} \log p_t(\mathbf{x}_t)$ of $p_t(\mathbf{x}_t)$. Using a time-dependent neural network $s_\theta(\mathbf{x}, t)$ called the score model, it is learned on X with denoising score matching. As described in [61] and [17], the score model is trained by approximating the known score functions of the transition distributions from \mathbf{x}_0 to \mathbf{x}_t , $p_{0t}(\mathbf{x}_t|\mathbf{x}_0)$. Optimized parameters θ^* ensure that $s_{\theta^*}(\mathbf{x}, t) \approx \nabla_{\mathbf{x}_t} \log p_t(\mathbf{x}_t)$ according to denoising score matching theory. The score model can then be plugged into Eq. (13), yielding:

$$d\mathbf{x}_t = [f(t)\mathbf{x}_t + g(t)^2 s_{\theta^*}(\mathbf{x}, t)] dt + g(t) d\bar{\mathbf{w}}_t \quad (14)$$

from here, one can sample from $p_0(\mathbf{x})$ using a sequence of time steps $0 = t_0 < t_1 < \dots < t_N = 1$ with standard iterative sampling techniques:

$$\mathbf{x}_{t_{i-1}} = \mathbf{h}(\mathbf{x}_{t_i}, \mathbf{z}_i, s_{\theta^*}(\mathbf{x}_{t_i}, t_i)) \quad (15)$$

where $\mathbf{z}_i \sim \mathcal{N}(\mathbf{0}, \mathbf{I})$ and \mathbf{h} denotes the iterative function related to the chosen sampling algorithm, such as annealed Langevin dynamics [11] or Predictor-Corrector samplers [17].

Conditioned sampling with SGMs (cSGM)

Although it is natural to *unconditionally* sample from Eq. (14), conditioning the sampling process to measurements, i.e. being able to sample from the posterior distribution $p(\mathbf{x}|\mathbf{y})$, is not trivial. Building on the unconditional case, Song et al. [25] introduce perturbed measurements \mathbf{y}_t given the experimental observation \mathbf{y} . They design an iterative sampling algorithm that promotes, at each time-step t_i , consistency of *conditioned* samples \mathbf{x}'_{t_i} simultaneously with the perturbed measurements \mathbf{y}_{t_i} and the *unconditioned* samples \mathbf{x}_{t_i} by solving a proximal optimization step:

$$\mathbf{x}'_{t_i} = \arg \min_w \{ (1 - \lambda) \|w - \mathbf{x}_{t_i}\|_{\mathcal{T}_{\phi_e}}^2 + \lambda \min_u \|w - u\|_{\mathcal{T}_{\phi_e}}^2 \} \quad s.t. \quad \mathcal{T}_{\phi_e}(u) = \mathbf{y}_{t_i} \quad (16)$$

where \mathcal{T}_{ϕ_e} is the Radon transform sampled on ϕ_e , the set of experimental viewing angles, and $\|\cdot\|_{\mathcal{T}}^2 = \|\mathcal{T}(\cdot)\|_2^2$. More details on the Radon transform and CT can be found in Appendix A. The hyper-parameter $\lambda \in [0, 1]$ balances consistency regarding experimental measurements ($\lambda \rightarrow 1$) and *unconditioned* samples ($\lambda \rightarrow 0$).

Song et al. [25] demonstrated that Eq. (16) has a tractable closed-form solution, such that in practice, *conditioned* samples are computed through:

$$\mathbf{x}'_{t_i} = \mathcal{T}_{\phi_e}^\dagger [P_{\phi_e}(\lambda \mathbf{y}_{t_i} + (1 - \lambda) \mathcal{T}_{\phi_e}(\mathbf{x}_{t_i})) + P_{\phi_s} \circ \mathcal{T}_{\phi_s}(\mathbf{x}_{t_i})] \quad (17)$$

where the set ϕ_e of experimental viewing angles is completed with simulated viewing angles ϕ_s to constitute an appropriate sampling, $\Phi = \phi_e \cup \phi_s$, above the Nyquist criterion, so that the inverse Radon transform \mathcal{T}_Φ^\dagger is well-defined. P denotes a profile padding operator ensuring dimensionality consistency.

Given *conditioned* samples \mathbf{x}'_{t_i} , at time-step t_i , the same iterative sampling strategy as Eq. (15) is applied to draw *unconditioned* samples $\mathbf{x}_{t_{i-1}}$:

$$\mathbf{x}_{t_{i-1}} = \mathbf{h}(\mathbf{x}'_{t_i}, \mathbf{z}_i, s_{\theta^*}(\mathbf{x}_{t_i}, t_i)) \quad (18)$$

where $s_{\theta^*}(\mathbf{x}, t)$ is the score model trained on X in an unsupervised manner, i.e. without assuming any measurement process. The reconstruction is ultimately computed by iterating sequentially on steps described in Eq. (18) and Eq. (17).

Manifold Constraint on the Gradient (MCG)

Chung et al. [26] refined this process by interpreting the diffusion process as a transport from the data manifold \mathbf{x}_0 to the hypersphere where pure noise is concentrated \mathbf{x}_1 through interpolating manifolds that correspond to the subsequent steps $0 < t < 1$. More specifically, given a discrete implementation of the diffusion process reparameterized as $\mathbf{x}_i = a_i \mathbf{x}_0 + b_i \mathbf{z}$ with $\mathbf{z} \sim \mathcal{N}(\mathbf{0}, \mathbf{I})$, the application of Tweedie’s formula [62] gives the following posterior expectation:

$$\hat{\mathbf{x}}_0 = \mathbb{E}[\mathbf{x}_0 | \mathbf{x}_i] = \frac{1}{a_i} (x_i + b_i^2 \nabla_{\mathbf{x}_i} \log p_i(\mathbf{x}_i)) \quad (19)$$

From here, Chung et al. [26] prove that, by assuming local linearity of the data manifold \mathcal{M} , it is possible to design a correction term for data fidelity that does not leave \mathcal{M} , yielding *corrected* samples:

$$\mathbf{x}_{t_i}^c = \mathbf{x}_t - \alpha \nabla_{\mathbf{x}_{t_i}} \|\mathbf{y}_{\phi_e} - \mathcal{T}_{\phi_e}(\hat{\mathbf{x}}_0)\|_2^2 \quad (20)$$

where α is a hyper-parameter, \mathbf{y}_{ϕ_e} and \mathcal{T}_{ϕ_e} are respectively the set of experimental measurements and the Radon transform sampled on experimental viewing angles. The *corrected* samples are additionally projected onto measurement space to further prevent deviation from data consistency. By applying subsequently the steps described in Eq. (19) and Eq. (20), MCG diffusion is guided to lie on the data manifold resulting in more faithful reconstruction compared to cSGM.

Appendix C: Effect of the interpolation factor

In this study, the impact of the number of experimental profiles provided during the optimization process described in Eq. (5) on reconstruction performances is examined. For this purpose, 5 independent reconstructions, one for each patient of the LIDC test set, are conducted for several interpolation factors: 4, 8, 16 and 64. Independently for each patient, the augmentation is achieved by inserting new artificial profiles computed by linear interpolation between the existing experimental profiles along the axis orthogonal to the slices plane. The interpolation factor corresponds to the number by which the initial profiles quantity is multiplied in the process. Reconstruction quality is evaluated using median PSNR values over the entire LIDC test set for varying experimental setups with: 9, 23 and 50 viewing angles. Reconstructions computed using artificial profiles are discarded. These quantitative metrics are given in figure 6 for two experiments, one with no prior training and the other with the decoder trained on the sub-dataset consisting of a 35% portion of the LIDC dataset.

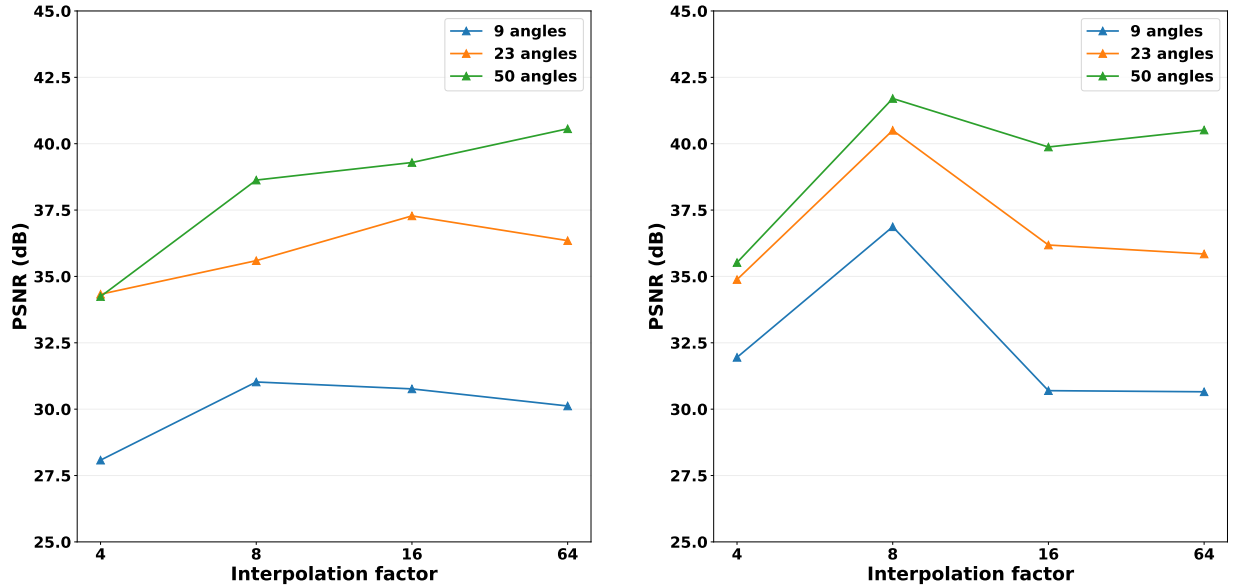


Figure 6: Median PSNR values for reconstructions of slices from the LIDC test set given : 9, 23 and 50 experimental viewing angles. They are obtained with cGLO without any training dataset (left) and trained on the 35% portion of the LIDC dataset (right).

The results presented in figure 6 indicate that the interpolation factor has a significant impact on reconstruction quality by inducing great variations (several dBs) for each curve, i.e. each experimental setup. Concerning experiments *with* prior unsupervised training, our model displays a consistent behavior across angles with a peak performance for a factor of 8. Also, a greater performance gap benefiting higher numbers of viewing angles can be observed for increasing interpolation factors both for experiments *with* and *without* prior training.

The interpolation factor used in our method can be seen as a hyper-parameter balancing the learned prior in Eq. (7), and the data-likelihood enforcing experimental profile consistency during the reconstruction task at examination time in Eq. (5). Indeed, for sufficiently important interpolation factors (greater than 16), performances *with* prior training become similar to those *without* any training. It implies that beyond a given interpolation factor value, decoder initialization, i.e. prior information learned on the unsupervised training sub-dataset, is completely overwritten by the second optimization.

Consequently the interpolation factor should be adapted for each use case, with higher values for experimental setups involving more viewing angles and a potential upper limit depending on the quantity of training data at hand.

Appendix D: Additional results tables

Method	Data	LIDC 320×320		LDCT 512×512	
		PSNR \uparrow	SSIM \uparrow	PSNR \uparrow	SSIM \uparrow
cSGM	2%	28.47 \pm 1.04	0.784 \pm 0.027	24.46 \pm 1.10	0.664 \pm 0.059
MCG	2%	33.05 \pm 1.35	<u>0.789</u> \pm 0.020	33.19 \pm 1.15	<u>0.814</u> \pm 0.033
cGLO	2%	<u>31.60</u> \pm 1.30	0.923 \pm 0.016	<u>30.53</u> \pm 0.98	0.903 \pm 0.014
cSGM	10%	29.25 \pm 1.00	0.800 \pm 0.020	26.91 \pm 1.08	0.744 \pm 0.041
MCG	10%	34.88 \pm 1.12	0.848 \pm 0.013	33.20 \pm 1.07	<u>0.821</u> \pm 0.024
cGLO	10%	35.31 \pm 0.94	0.957 \pm 0.008	<u>31.35</u> \pm 0.99	0.917 \pm 0.017
cSGM	35%	30.28 \pm 1.13	0.821 \pm 0.031	27.59 \pm 1.31	0.759 \pm 0.038
MCG	35%	35.45 \pm 1.19	<u>0.871</u> \pm 0.017	34.11 \pm 1.11	<u>0.841</u> \pm 0.019
cGLO	35%	<u>35.11</u> \pm 0.97	0.958 \pm 0.006	<u>31.19</u> \pm 1.08	0.913 \pm 0.016

Table 3: PSNR and SSIM median \pm half Inter Quartile Range (IQR) values for reconstructions of slices from the LIDC and the LDCT test datasets given 9 experimental viewing angles. Best and second best results are respectively indicated as bold and underline for each sub-dataset and metric.

Method	Data	LIDC 320×320		LDCT 512×512	
		PSNR \uparrow	SSIM \uparrow	PSNR \uparrow	SSIM \uparrow
cSGM	2%	33.89 \pm 1.01	0.879 \pm 0.019	29.09 \pm 0.61	0.793 \pm 0.018
MCG	2%	<u>36.55</u> \pm 1.23	<u>0.888</u> \pm 0.012	35.76 \pm 1.41	<u>0.871</u> \pm 0.015
cGLO	2%	37.60 \pm 1.67	0.972 \pm 0.009	<u>35.68</u> \pm 1.03	0.955 \pm 0.010
cSGM	10%	36.31 \pm 0.79	0.912 \pm 0.015	33.35 \pm 1.02	0.887 \pm 0.017
MCG	10%	38.92 \pm 0.92	0.923 \pm 0.010	36.45 \pm 1.28	0.879 \pm 0.013
cGLO	10%	39.82 \pm 1.26	0.981 \pm 0.006	37.34 \pm 1.40	0.967 \pm 0.010
cSGM	35%	36.62 \pm 1.61	0.916 \pm 0.024	34.90 \pm 1.08	0.907 \pm 0.015
MCG	35%	<u>39.60</u> \pm 1.17	<u>0.933</u> \pm 0.014	38.58 \pm 1.37	<u>0.910</u> \pm 0.013
cGLO	35%	39.85 \pm 1.19	0.982 \pm 0.005	<u>36.61</u> \pm 1.45	0.962 \pm 0.010

Table 4: PSNR and SSIM median \pm half Inter Quartile Range (IQR) values for reconstructions of slices from the LIDC and the LDCT test datasets given 23 experimental viewing angles. Best and second best results are respectively indicated as bold and underline for each sub-dataset and metric.

Method	Data	LIDC 320×320		LDCT 512×512	
		PSNR \uparrow	SSIM \uparrow	PSNR \uparrow	SSIM \uparrow
cSGM	2%	36.90 \pm 0.83	<u>0.922</u> \pm 0.016	32.46 \pm 0.56	0.867 \pm 0.015
MCG	2%	<u>37.92</u> \pm 0.85	0.909 \pm 0.008	<u>37.01</u> \pm 1.46	0.894 \pm 0.009
cGLO	2%	40.50 \pm 1.56	0.983 \pm 0.007	38.24 \pm 1.05	0.972 \pm 0.007
cSGM	10%	<u>40.03</u> \pm 1.05	<u>0.950</u> \pm 0.016	36.78 \pm 0.96	0.937 \pm 0.013
MCG	10%	40.02 \pm 1.10	0.936 \pm 0.009	38.55 \pm 1.38	0.913 \pm 0.011
cGLO	10%	41.45 \pm 1.53	0.985 \pm 0.006	39.73 \pm 1.31	0.979 \pm 0.007
cSGM	35%	40.04 \pm 1.45	0.950 \pm 0.019	38.37 \pm 1.05	0.953 \pm 0.010
MCG	35%	<u>40.79</u> \pm 1.21	0.943 \pm 0.008	39.81 \pm 1.42	0.939 \pm 0.010
cGLO	35%	40.89 \pm 1.38	0.984 \pm 0.006	<u>39.48</u> \pm 1.43	0.978 \pm 0.008

Table 5: PSNR and SSIM median \pm half Inter Quartile Range (IQR) values for reconstructions of slices from the LIDC and the LDCT test datasets given 50 experimental viewing angles. Best and second best results are respectively indicated as bold and underline for each sub-dataset and metric.

Appendix E: Additional reconstruction examples

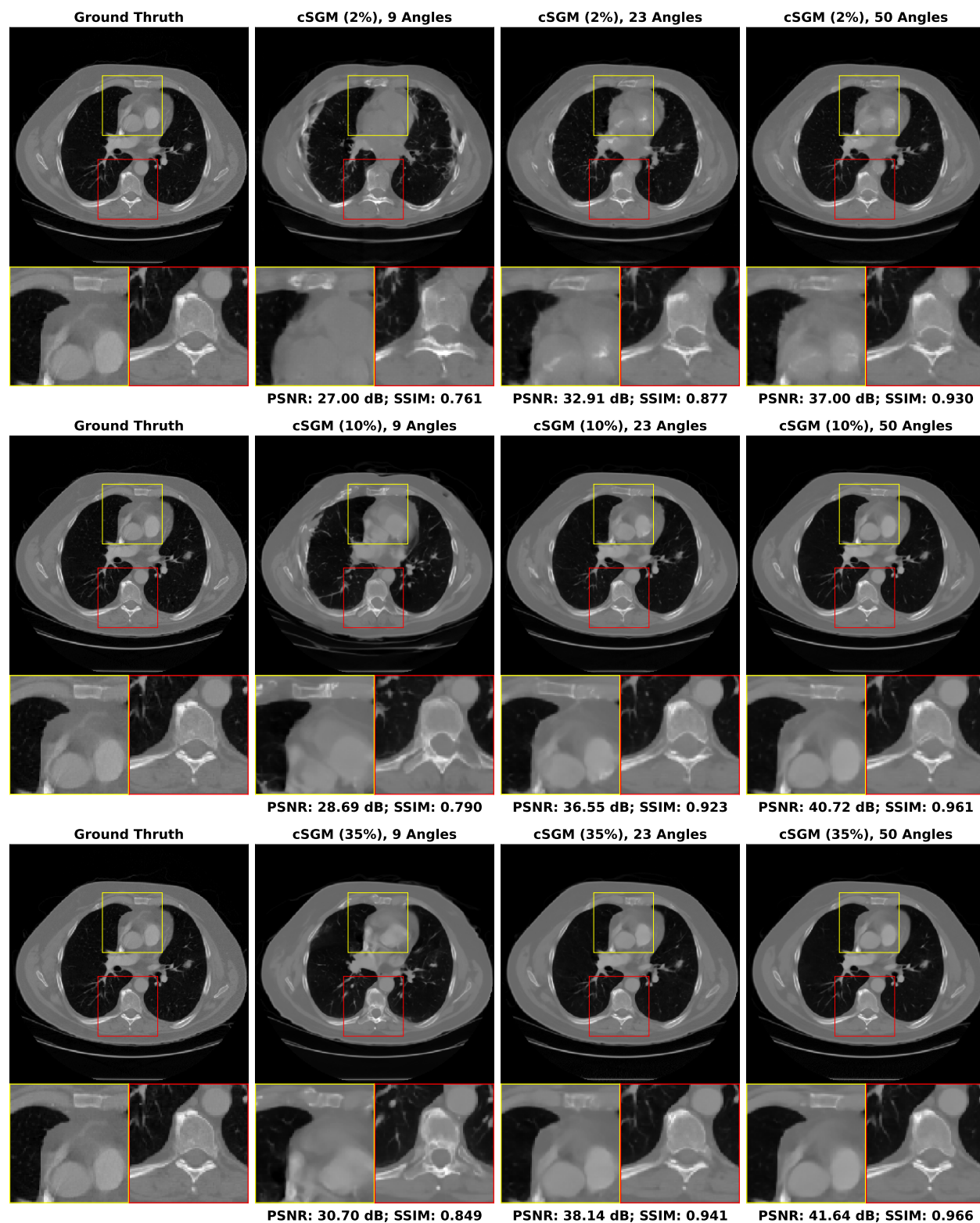


Figure 7: Examples of reconstructions of slices from the LIDC test set given : 9, 23 and 50 experimental viewing angles. They are obtained with cSGM trained on the 2%, 10% and 35% LIDC sub-datasets.

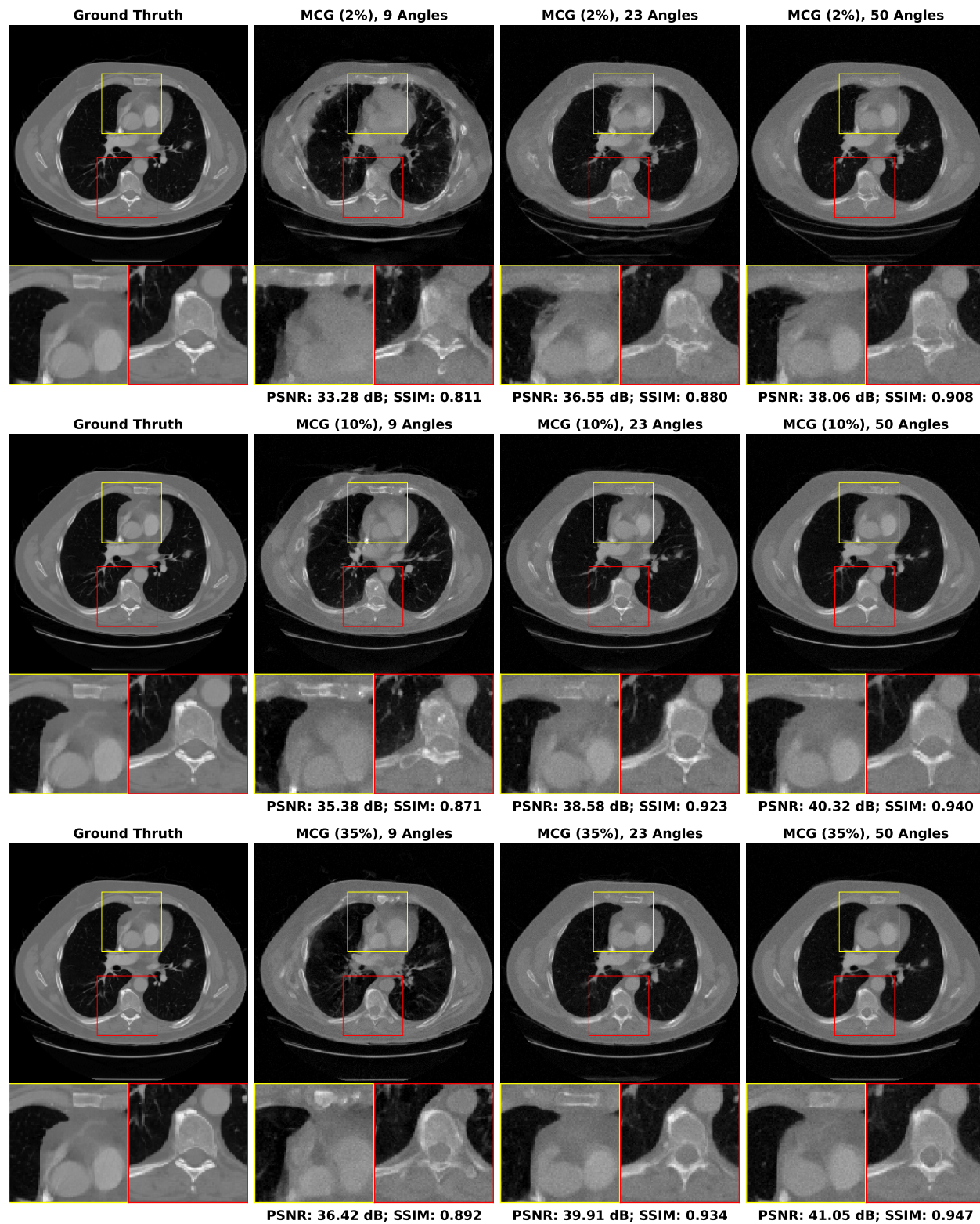


Figure 8: Examples of reconstructions of slices from the LIDC test set given : 9, 23 and 50 experimental viewing angles. They are obtained with MCG trained on the 2%, 10% and 35% LIDC sub-datasets.

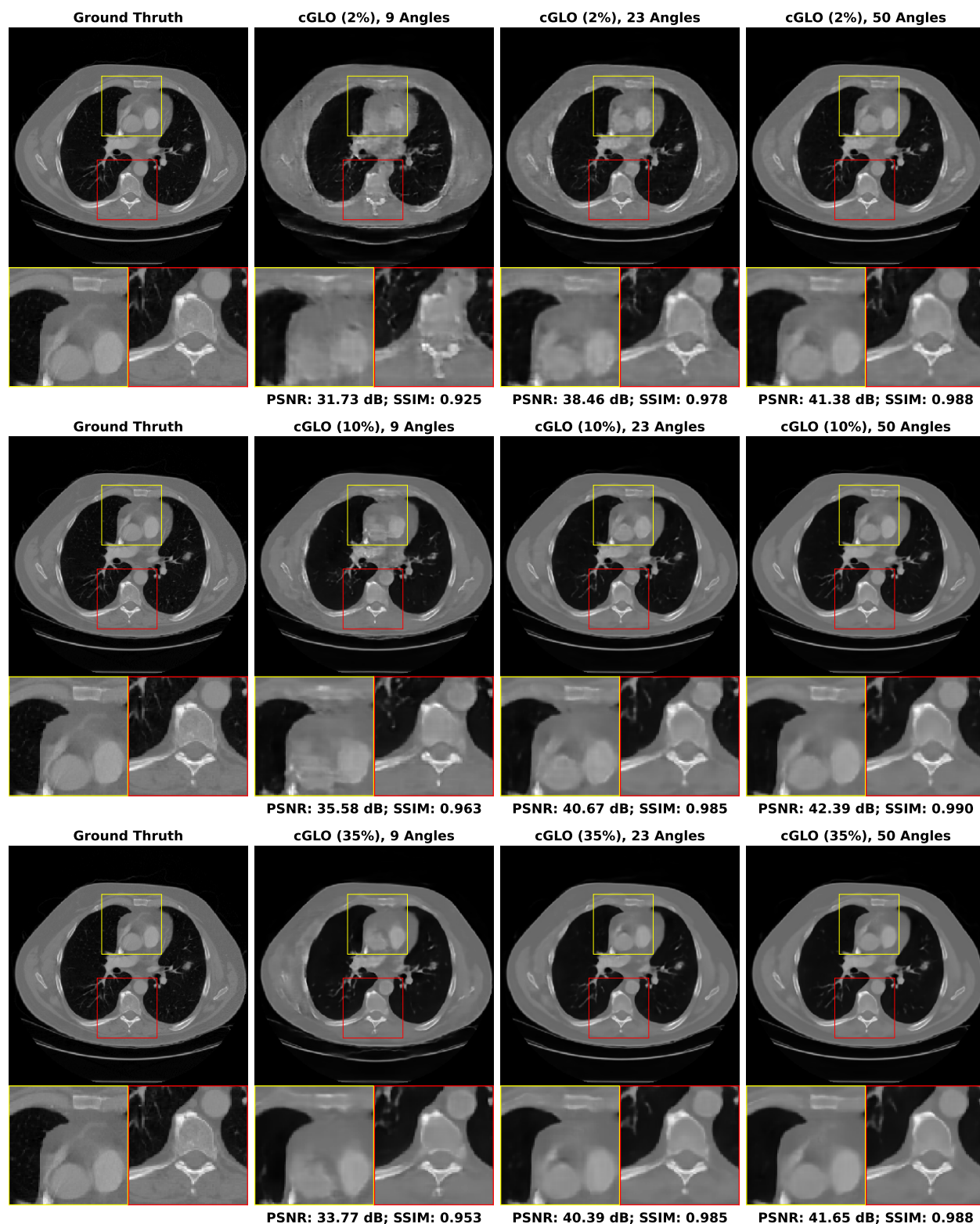


Figure 9: Examples of reconstructions of slices from the LIDC test set given : 9, 23 and 50 experimental viewing angles. They are obtained with cGLO trained on the 2%, 10% and 35% LIDC sub-datasets.